MONTE CARLO MODELING OF AN X-RAY FLUORESCENCE

DETECTION SYSTEM BY THE MCNP CODE

A Thesis
Presented to
The Academic Faculty

By

Fang Liu

In Partial Fulfillment
Of the Requirements for the Degree
Master of Science in Medical Physics in the
School of Mechanical Engineering

Georgia Institute of Technology
May 2009

MONTE CARLO MODELING OF AN X-RAY FLUORESCENCE

DETECTION SYSTEM BY THE MCNP CODE

Approved by:

Dr. Sang Hyun Cho, Advisor
Nuclear & Radiological Engineering and Medical
Physics, School of Mechanical Engineering
Georgia Institute of Technology

Dr. Farzad Rahnema
Nuclear & Radiological Engineering and Medical
Physics, School of Mechanical Engineering
Georgia Institute of Technology

Dr. Chris Wang
Nuclear & Radiological Engineering and Medical
Physics, School of Mechanical Engineering
Georgia Institute of Technology

Date Approved: Dec. 5, 2008

ACKNOWLEDGEMENTS

TABLE OF CONTENTS

LIST OF FIGURES

SUMMARY

An X-ray fluorescence detection system has been designed by our research group for quantifying the amount of gold nanoparticles presented within the phantom and animals during gold nanoparticle-aided cancer detection and therapy procedures. The primary components of the system consist of a micro-focus X-ray source, a Pb beam collimator, and a CdTe photodiode detector. In order to optimize and facilitate future experimental tasks, a Monte Carlo model of the detection system has been created by using the MCNP5 code. Specifically, the model included an X-ray source, a Pb collimator, a CdTe detector, and an acrylic plastic phantom with four cylindrical columns where various materials such as gold nanoparticles, aluminum, etc. can be inserted during the experiments. In this model, X-rays from a micro-focus source with the nominal tube voltage of 110 kVp emitted into a 60° cone were collimated to a circular beam with a diameter of 5 mm. The collimated beam was then delivered to the plastic phantom with and without a gold nanoparticle-containing column. The fluence of scattered and gold fluorescence X-rays from the phantom was scored within the detector's sensitive volume resulting in various photon spectra and compared with the spectra acquired experimentally under the same geometry. The results show that the current Monte Carlo model can produce the results comparable to those from actual experiments and therefore it would serve as a useful tool to optimize and troubleshoot experimental tasks necessary for the development of gold nanoparticle-aided cancer detection and therapy procedures.

CHAPTER 1

INTRODUCTION

Cancer is one of the public leading causes of death in the world. Accordingly, diagnostics and therapeutics of cancers are active areas of research today. A recent explosion in engineering——nanotechnology that involves the design and engineering of objects <100 nanometers (nm) in size offers an extraordinary, paradigm-changing opportunity to make significant advances in cancer diagnosis and treatment [1]. For example, by conjugating, or binding, the gold nanoparticles to an antibody for a specified receptor on the surface of the tumor cell, researchers were able to attach gold nanoparticles to the tumor cells. The photon scatter and absorption properties of tumor cells attached to gold nanoparticles could be quite different from those of normal cells and, as a result, provide a unique opportunity for cancer imaging and therapy. For example, cancerous cells could be detected by detecting the fluorescence X-rays from gold nanoparticles during X-ray irradiation and/or destroyed much more effectively by taking advantage of increased energy deposition (i.e., dose enhancement) to tumor cells due to photoelectrons originated from gold nanoparticles attached to tumor cells [2].

The Monte Carlo method is widely used for solving problems involving the random walk process. In particular, it is employed in the modeling of nuclear medical imaging systems, due to the stochastic nature of radiation emission and transport, and of detection processes. By using the Monte Carlo method, new imaging techniques and devices can be simulated accurately under the realistic clinical condition without conducting experiments in living subjects. Image quality can be improved by analyzing the image formation procedure with detailed physical interaction mechanisms.

Many Monte Carlo user codes have existed for radiation simulation. One of the most popular codes in the public domain is the MCNP (Monte Carlo N-Particle) code that can simulate radiation transport of neutron, photon, electron, or coupled neutron/photon/electron. Specific areas of application include medical imaging, radiation protection and dosimetry, radiation shielding, radiography, and medical physics. Also, some other codes are available for the Monte Carlo simulation, such as EGSnrc (Electron Gamma Shower – National Research Council of Canada), a general purpose code based on the popular EGS4 system that incorporates a variety of improvements, was shown to produce artifact-free condensed history simulation of coupled electron/photon transport. The simulation results between MCNP and EGSnrc are similar but not identical. In this work, we use the MCNP code, since it offers a more sophisticated general source definition and is more flexible when specifying the simulation geometry [3]. In order to perform the MCNP simulation, detailed information on the imaging system characteristics such as source beam energy and direction, detector configuration and position, phantom material and geometry is needed. Once the model for an imaging system is created, the MCNP code simulates the physical processes by bombarding billions of randomly sampled source particles towards the phantom and scoring the tally results by following every particle of interest.

In this work, an X-ray fluorescence detection system has been created by using the MCNP5 code. An X-ray source, a Pb collimator, a CdTe detector, and an acrylic plastic phantom with four empty cylindrical columns are included in this model. Various materials such as gold nanoparticles, aluminum, etc. can be inserted into the four cylindrical columns during the experiments. In the simulation, 110 kVp X-rays emitted

into a 60° cone from the focal spot of the X-ray source was collimated to a circular beam with a diameter of 5 mm. The collimated beam was then delivered to the plastic phantom with and without a gold nanoparticle-containing column. The fluence of scattered and gold fluorescence X-rays from the phantom was scored within the detector's sensitive volume resulting in various photon spectra which were compared with the measured spectra acquired under the same geometry. The current MCNP model may serve as a useful simulation tool to optimize and troubleshoot experimental tasks necessary for the development of gold nanoparticle-aided cancer detection and therapy procedures.

CHAPTER 2

METHOD AND METERIALS

2.1 The Physics of X-ray Fluorescence

When materials are exposed to short-wavelength X-rays or to gamma rays, ionization of their component atoms may take place. Ionization consists of the ejection of one or more electrons from the atom, and may take place if the atom is exposed to radiation with energy greater than its ionization potential. X-rays and gamma rays can be energetic enough to expel tightly-held electrons from the inner orbital of the atom. The removal of an electron in this way renders the electronic structure of the atom unstable, and electrons in higher orbital "fall" into the lower orbital to fill the hole left behind. In this type of falling, energy is released in the form of a photon, the energy of which is equal to the energy difference of the two orbital involved. Thus, the material emits radiation, which has energy characteristic of the atoms present. The term fluorescence is applied to phenomena in which the absorption of higher-energy radiation results in the re-emission of lower-energy radiation [4].

Each element has electronic orbital of characteristic energy. Following the removal of an inner electron by an energetic photon provided by a primary radiation source, an electron from an outer shell drops into its place. There are a limited number of ways in which this can happen, as shown in figure 2.1. The main transitions are given names: an L→K transition is traditionally called Kα, an M→K transition is called Kβ, and an M→L transition is called Lα, and so o n Each of these transitions y ield s a fluorescent photon with a characteristic energy equal to the difference in energy of the

initial and final orbital [4]. The wavelength of this fluorescent radiation can be calculated from Planck's Law: λ=h · c / E.
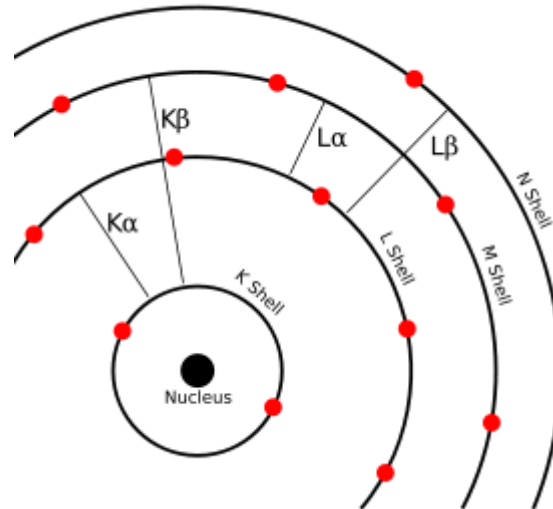
Figure 2.1: Electronic transitions in a calcium atom [4]

Analysis using X-ray fluorescence is called "X-ray Fluorescence Spectroscopy." The fluorescent radiation can be analyzed either by sorting the energies of the photons (energy-dispersive analysis) or by separating the wavelengths of the radiation (wavelength-dispersive analysis). Once sorted, the intensity of each characteristic radiation is directly related to the amount of each element in the material.

2.2 Introduction to Monte Carlo Method and MCNP Codes

2.2.1 Monte Carlo Methods

Numerical methods that are known as Monte Carlo methods can be loosely described as statistical simulation methods, where statistical simulation is performed with repeated random sampling and the average of the simulated results approach the true value as the number of sampling points becomes large [5].

Monte Carlo methods are often used when it is infeasible or impossible to compute an exact result with a deterministic algorithm and also when solving physical and mathematical problems involving statistical process. In particular, it is employed in the modeling of nuclear medical imaging and detection systems, due to the stochastic nature of radiation emission and transport, and of detection processes. The method is very useful for complex problems that cannot be modeled analytically or when experimental measurements may be impractical. Also, simulation yields "perfect knowledge" of photon histories. With MC codes, new nuclear medical imaging and detection techniques and devices can be investigated accurately under realistic situations without conducting experiments in living subjects. Image quality can be improved by analyzing the results from MC simulations [6].

2.2.2 MCNP Code

The Monte Carlo method was developed at Los Alamos during the Manhattan Project in the early 1940s. The current MCNP code is the heir to those early efforts. The first multipurpose code version was written in 1963. In the mid-70's, neutron and photon codes were merged to form MCNP, which has undergone major upgrades approximately every two to three years since. MCNP3 was released in 1983 and rewritten in standard FORTRAN. MCNP4 was released in July 1990 at Los Alamos and in March 1991 to the Reactor Shielding and Information Center at Oak Ridge (version MCNP4.2). Hundreds of minor improvements in the following years added up to the current MCNP5 edition which was released to ORNL/RSICC and made available to people within the US in April 2003 [7].

MCNP is a general-purpose <u>M</u>onte <u>C</u>arlo <u>N</u>-<u>P</u>article code that can be used for neutron, photon, electron, or coupled neutron/photon/electron transport [6]. It provides very convenient and versatile source definition, geometry configuration and numerous flexible tallies. It enables the most accurate radiation transport calculations for various problems including radiotherapy and imaging problems. It simulates the physical processes by bombarding a large number (e.g., billions) of randomly sampled source particles towards the phantom and scoring the tally results by following every particle of interest. Typically, less than 5% statistic errors are permitted for the reasonable results and sometimes to reach the acceptable level would cost a lot of computer running time.

2.3 The X-ray Source and Fluorescence Detector

2.3.1 The Micro-Focus X-ray Source

The current work was performed with Hamamatsu L9631 micro-focus X-ray source, a compact X-ray generator operating at a maximum tube voltage of 110 kVp and a maximum tube current of 800 μA. The maximum X-ray emission angle is 62° and the minimum focal spot size for the output beam is 15 μm. The L9631 consists of three components: a micro-focus X-ray tube, a high-voltage generator circuit and a control circuit, which are integrated into a single unit. The L9631 can be operated and controlled from an external control unit (PC, etc.). The picture below in Figure 2.2 shows the L9631 micro-focus X-ray source used for the current work. The X-ray beam comes out of a circular beryllium window shown as a circular metal plate in Figure 2.2 [9].

Figure 2.2: Hamamatsu L9631 Micro-Focus X-ray Source

2.3.2 The CdTe Photodiode Detector

The CdTe Photodiode Detector used for this work was Model XR-100T-CdTe (manufactured by Amptek, Inc.) which is a high performance X-ray and gamma ray detector, preamplifier, and cooler system using a 3 x 3 x 1 mm Cadmium Telluride (CdTe) diode detector mounted on a two-stage thermoelectric cooler. Also on the cooler are the input field-effect transistor (FET) feedback components to the charge sensitive preamplifier. The internal components are kept at approximately -30ºC and can be monitored by a temperature sensitive integrated circuit. The hermetic TO-8 package of the detector has a light tight, vacuum tight 4 mil (100 µm) Beryllium window [10]. The current MCNP model for this detector includes only the head of the detector beginning from the outermost beryllium window to the CdTe diode detector. The detailed view for the detector is shown in the right panel of Figure 2.3.
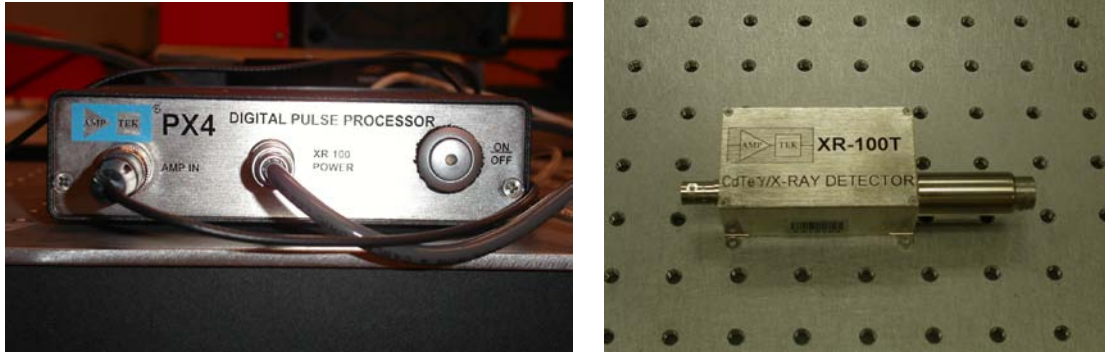
Figure 2.3: The XR-100T-CdTe Photodiode Detector System

2.4 The Phantom

A design developed by our research group was employed to produce a solid tissue-equivalent phantom in the form of a cylindrical block, 48 mm in length and 50 mm in diameter, as illustrated in Figure 2.4. The material we used for the block was a transparent plastic known as Polymethyl Methacrylate (or PMMA) with the molecular formula of $(C_5O_2H_8)n$ which is very compatible with the human tissue. Inserted within the block are eight small cylinders, four of which in the top side are of the same size (25 mm in length, 10.5 mm in diameter) and centered 15 mm off from the central axis. The other four in the bottom side are 15 mm in length and 4.3 mm in diameter, which are centered 12.7 mm off from the central axis. These top cylinders are used to hold a column filled with a mixture of gold nanoparticles (1.9 nm diameter) and water as can be seen in Figure 2.5.

Top view

50 mm

15 mm | 15 mm

10.5 mm

Material: PMMA

Bottom view

0.50' (12.7 mm)

4.3 mm

Side view

15 mm

10.5 mm

25 mm

48 mm

15 mm

0.50' (12.7 mm)   4.3 mm

10 mm

25 mm

Material: Al X 4

Material: PMMA X 4

10 mm

5 mm

Material: PMMA X 4

Threaded part: #8-32
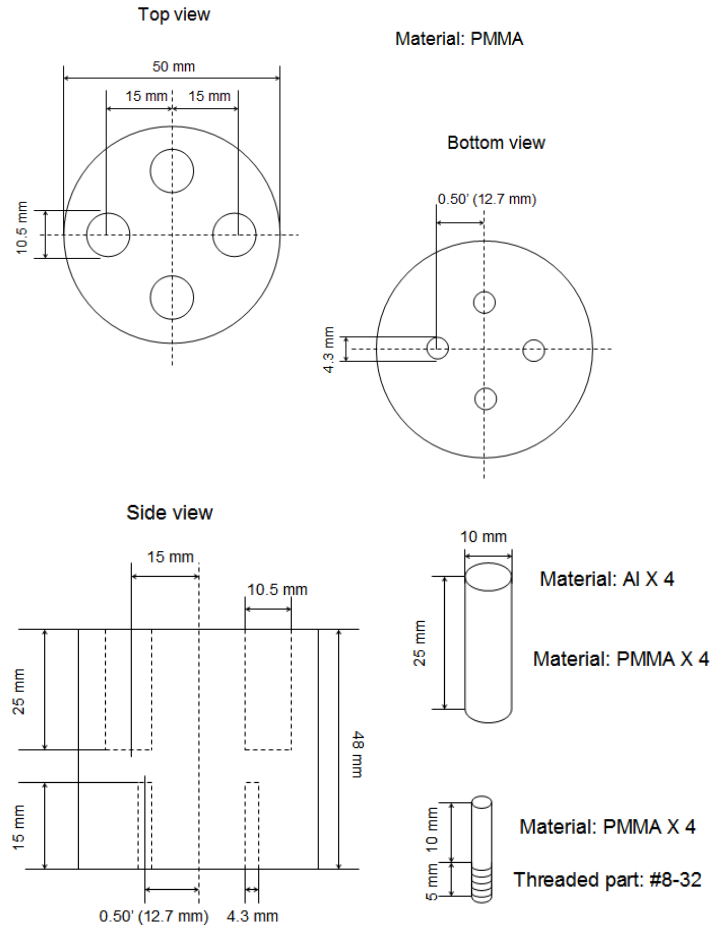
Figure 2.4: Schematic diagram of the cylindrical solid tissue-equivalent phantom

(a)

(b)
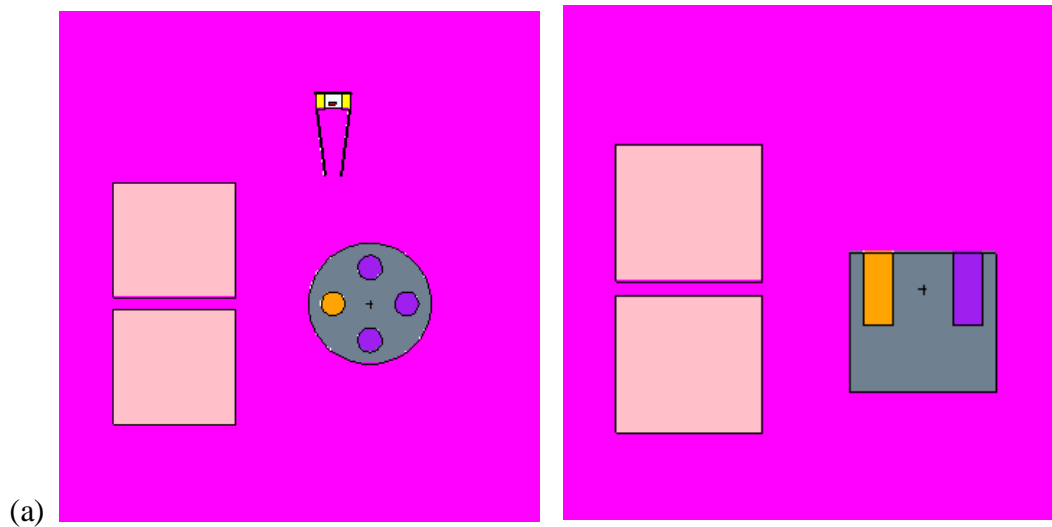
Figure 2.5: (a) Two different cross-sectional views of the MCNP model of gold X-ray fluorescence detection system (b) the column containing a mixture of gold nanoparticles and water which would be inserted into the phantom

2.5 The MCNP Modeling

A Monte Carlo model of the detection system has been created by using the MCNP5 code and the pulse height tally, F8, was used in this work for the photon scoring. Specifically, the model includes all of the components described in the previous sections. The shape and dimension for all the parts in the model were based on the manufacturers' specifications and our original design. The geometry section in the MCNP input file can be divided to three parts —— the CdTe photodiode detector, the micro-focus X-ray source, and the phantom. After assuming negligible effect for calculations due to the absence of the electrical parts, cooling system, and the holding stand in the current MCNP model, we only modeled part of the head of the detector including the 4 mil (100 μm) Beryllium window, the CdTe diode detector (the red part in the cross-sectional view of the MCNP detector model in Figure 2.6), the nickel outwear cover (the yellow part),

11

the kovar-made bottom (the green part), and the white area around the detector completely filled with Nitrogen. According to the specifications for the micro-focus X-ray source, we biased an isotropic point source to a 60° cone beam and a 10 cm x 10 cm x 5 cm Pb block centered with a cylindrical hole was used to collimate the source X-rays to a circular beam with a diameter of 5 mm. The collimated beam was then delivered to the PMMA plastic phantom with and without a gold nanoparticle-containing column as shown in Figure 2.8. Some other components such as the source filter and detector collimator were also modeled for the current work.
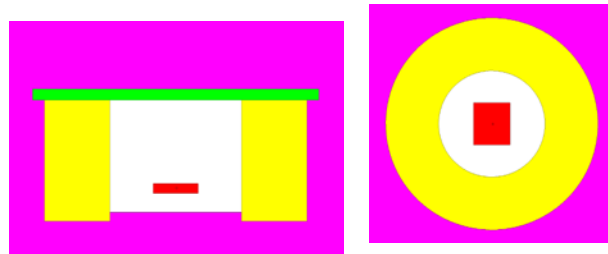
Figure 2.6: Two different cross-sectional views of the detector head

a   b
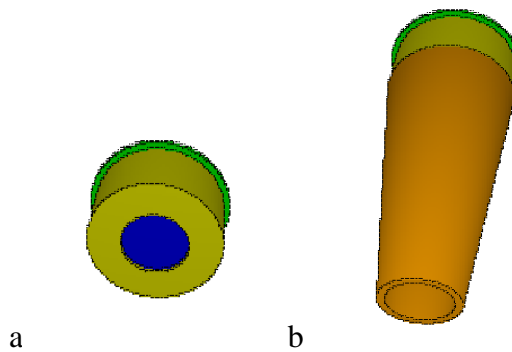
Figure 2.7: Three dimensional views of the MCNP detector model (a) without and

(b) with cone-shaped Pb collimator

a   b
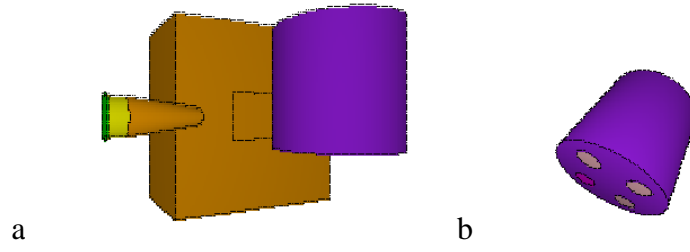
Figure 2.8: Three dimensional views of (a) the MCNP model for the whole

system and (b) the MCNP model of the PMMA phantom

CHAPTER 3

RESULTS

The MCNP model described in a previous chapter was used to predict the performance of our X-ray fluorescence system. The tally quantities in all of the specific tasks were the number of photons detected by the detector model. By analyzing the energies of detected photons, we were able to plot each X-ray spectrum with the gold fluorescence X-ray peaks. We performed this task by dividing our tally into 100 energy bins from 1kev to the maximum energy (e.g., 110kev) with 1kev interval. The results we acquired were compared with those from measurements. Below are the detailed results.

3.1 Modeling of X-ray Fluorescence System

In this part of simulation, we validated our MCNP model including the source, the detector, and the phantom. In order to improve the efficiency of the simulation, we needed to modify the source so that more statistically stable results could be obtained for gold fluorescence peaks.

3.1.1 The Source

The original cone beam source was a 60° cone beam source biased from an isotropic point source. The vendor of the current X-ray source suggested that we could use either 100 kVp or 150 kVp spectra (both are vendor-measured spectra) for the simulation with 110 kVp X-rays, as they do not have any measured spectrum for the 110 kVp source we have. Based on our own experimental measurements of scattered photon energy, we found that the end point energy of primary photons was significantly higher

than 110 keV. Therefore, we decided to use the 150 kVp spectrum as our source spectrum for the current simulation. Note the direct measurements of the primary spectrum for the 110 kVp source was somewhat beyond the scope of the current work. In any case, by using a cone beam source, the statistical error of the tally values was typically unacceptable even after running particle histories on the order of 1 billion. To improve the statistical error, significantly more histories, possibly by several orders of magnitude larger than 1 billion, were needed. However, it was impractical to run such large numbers of particle histories, especially when we needed to run several different jobs using the same source. To solve this problem, we scored the photon spectrum within a thin disk volume placed right after the source collimator hole using the same bin size and energy range as the original cone-beam X-ray source. Since we could not have enough photons to be collected within this area as explained earlier, the simulation was repeated for 7 times and the results were averaged for each bin to improve the statistical error to the range less than 8%. This averaged spectrum was used for the new disk source as a source spectrum. Figure 3.1 is the result of the comparison between the new spectrum and the original spectrum. We can see the new spectrum is almost the same as the original one, since only photons of the primary beam coming out directly through the collimator hole were scored and very few scattered photons from the collimator could be detected. So we used the same energy spectrum for the disk source replacing the original cone beam source and obtained much more stable results using the same number of histories. As illustrated in Figure 3.2, we used two different sources for the same MCNP model with a PMMA phantom. As we can see, the model with the disk source displayed much smoother curve with much more counts than that with the biased cone beam

source. Besides, in the later part of the simulation, we added a Pb filter for the disk source to absorb most of the low-energy photons in order to get more prominent gold fluorescence X-ray peaks. Figure 3.3 is the energy spectrum for the filtered disk source. Since a less number of low energy photons below the gold k-edge (~ 80keV) was originated from the filtered disk source, an identification of the gold fluorescence peaks became easier due to less scatter around the gold fluorescence peaks (e.g., 67kev).
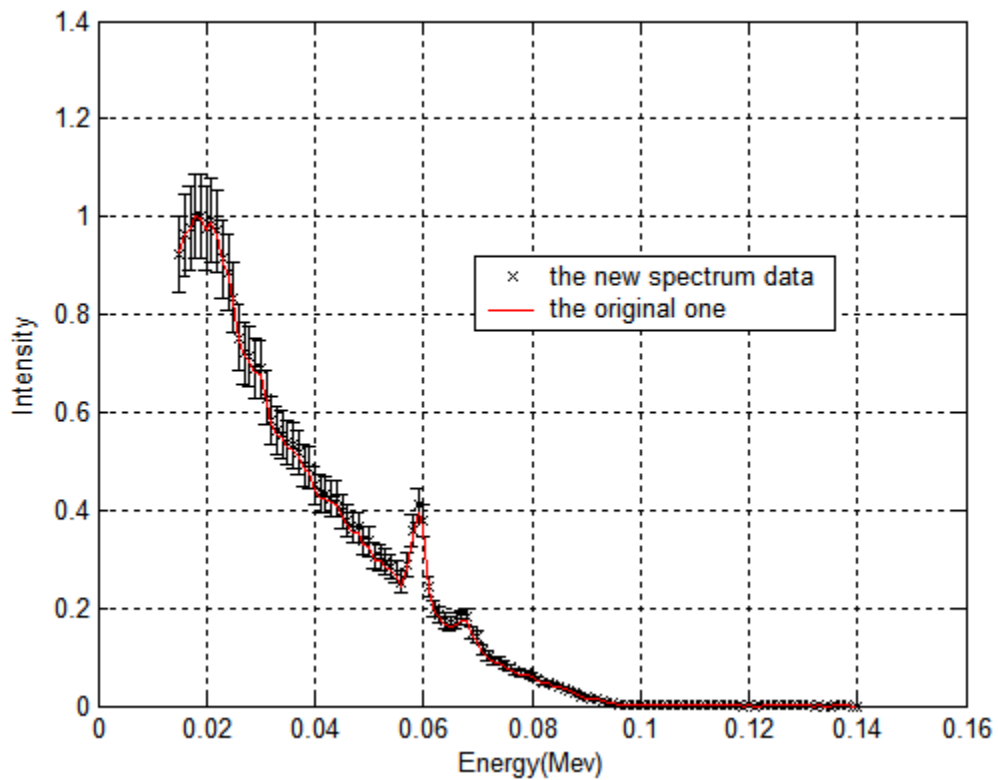
Figure 3.1: Comparison of the new disk source energy spectrum with the original energy spectrum
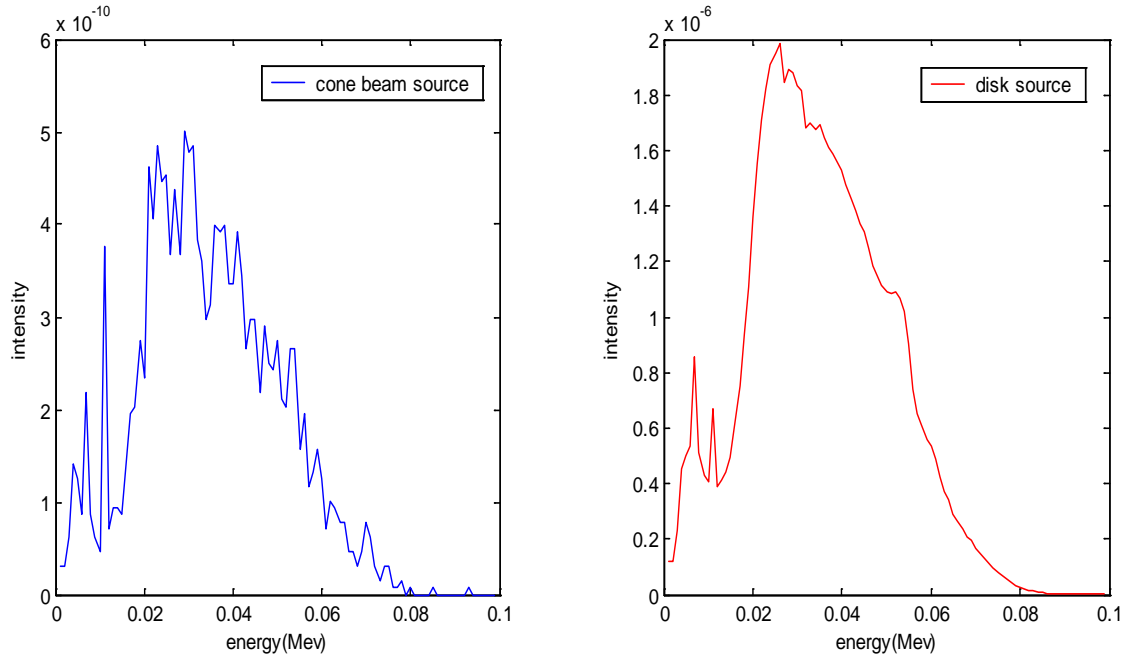
Figure 3.2: Detected spectra for the same MCNP model using different sources (The left-

side is for cone beam source while the right-side is for disk source)
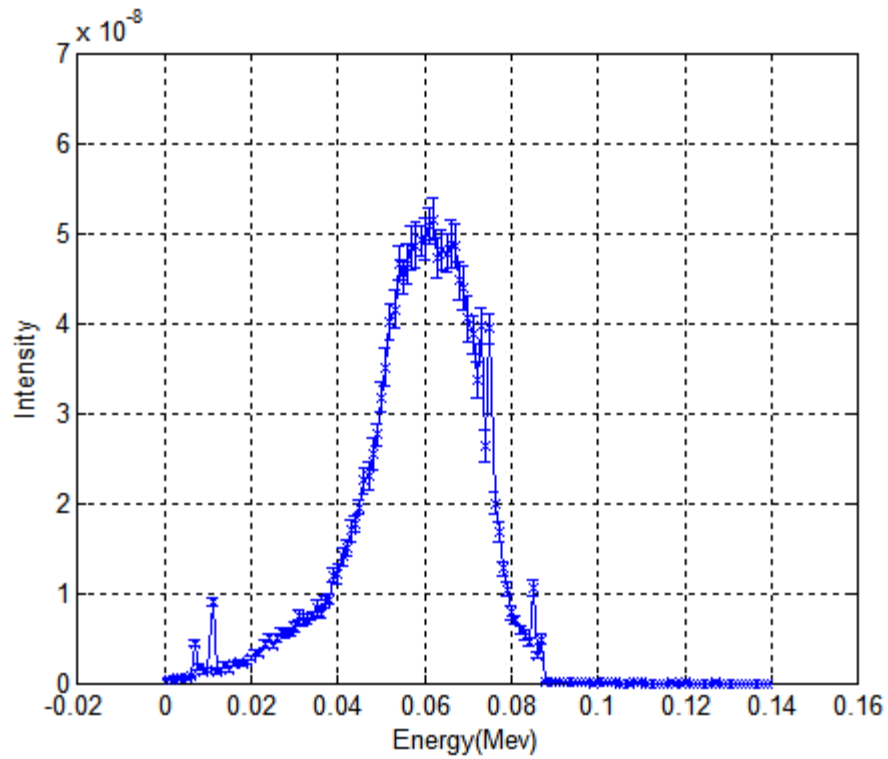
Figure 3.3: Energy spectrum with error bar for the filtered disk source

17

3.1.2 The Detector

We filled one of the cylindrical columns in the phantom with a mixture of gold nanoparticles and water and pointed our detector head directly at the gold column. Figure 3.4 below illustrates the normalized spectra we detected using two different gold concentrations of the columns (1% and 2%) with an un-collimated detector and the 2% gold column with a collimated detector. As we can see from the result, the detector we modeled was able to detect the gold fluorescence peaks in the spectra for both 1% and 2% gold columns resulting in higher gold peaks for a higher gold concentration. Besides, the spectrum obtained with a collimated detector produced much more prominent gold peaks than that obtained with an un-collimated detector for the same concentration of gold column, because of the discrimination of the scattered photons coming out of the phantom by the detector collimator.
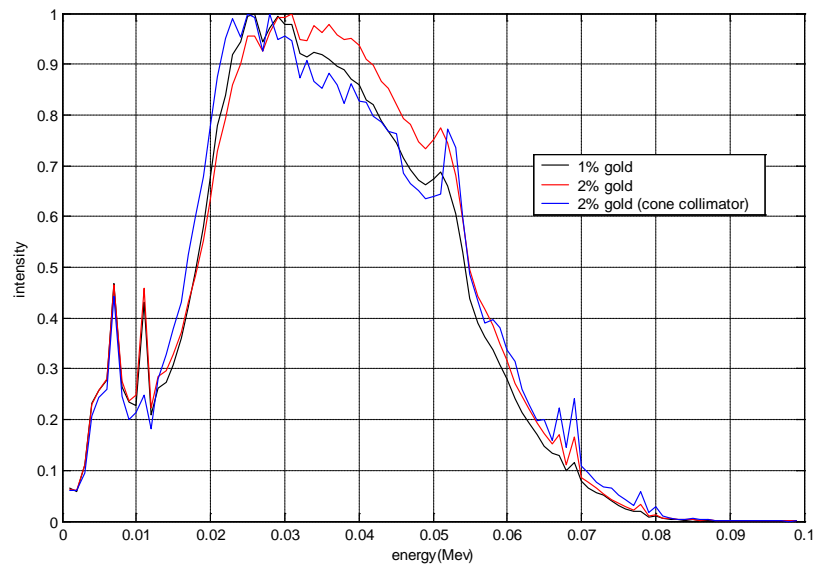
Figure 3.4: Normalized detected spectra for different concentrations of the gold columns (1% and 2%) using un-collimated detector and the 2% gold column using collimated detector

3.1.3 The Phantom

We filled our MCNP phantom model with different materials (PMMA, water, 1% gold, 2% gold) to investigate the photon scattering and attenuation effects of the phantom. Figure 3.5 shows the spectra detected using the phantoms with these different materials and the unfiltered disk source. As we can see from the results, the spectrum for PMMA phantom is very close to that for the water phantom and this phantom using PMMA material has the least attenuation among all the materials in the energy range of our X-ray simulation. Also, we made the same test with a filtered disk source and the similar result was achieved. The spectra for a filtered disk source were plotted in Figure 3.6.
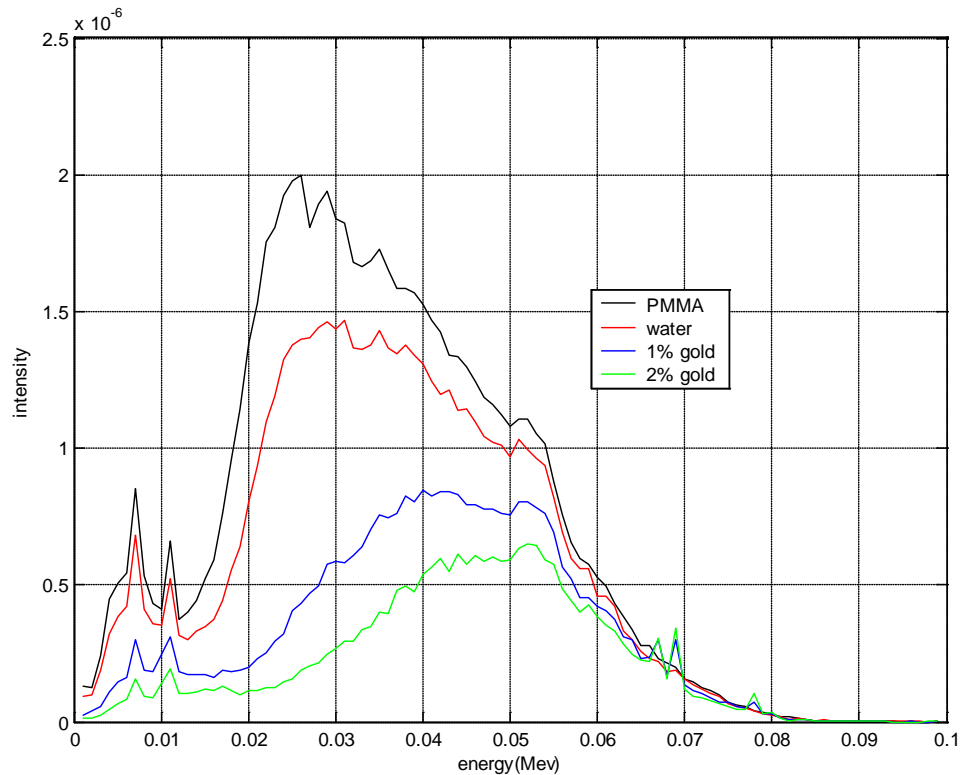
Figure 3.5: Spectra detected using the phantoms filled with different materials (unfiltered disk source)
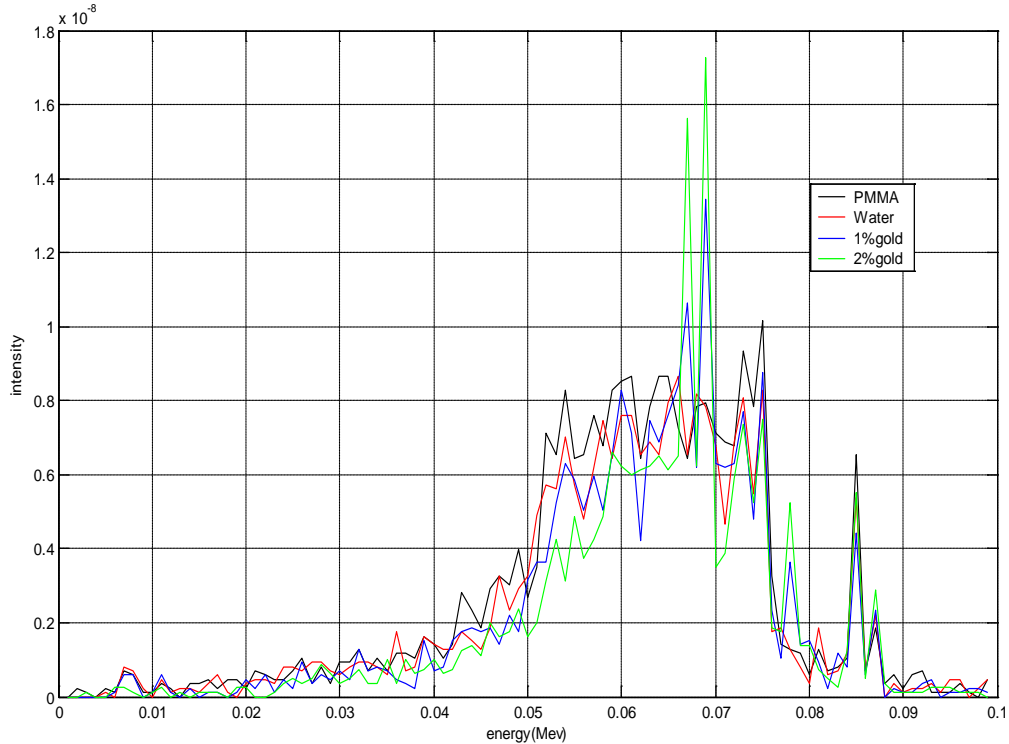
Figure 3.6: Spectra detected using the phantoms filled with different materials (filtered

disk source)

3.2 Effects of Various Parameters on Fluorescence Detection

In this part of simulation, we tried to optimize various parameters in our MCNP

model that could affect the fluorescence detection efficiency of the system by changing

the phantom to detector distance, the solid angle of the detector collimator, and the

detection angle for gold fluorescence spectrum. The simulation results were compared

with those from measurements to validate the current MCNP model for its future use as a

design tool for a more efficient fluorescence X-ray detection system.

3.2.1 The Solid Angle of the Detector Collimator

The spectra shown in Figure 3.7 and Figure 3.8 were acquired by using three

different sizes (0.65cm, 0.75cm and 0.85cm diameter) of the cone collimator opening

20

(i.e., solid angle) for the detector in our MCNP model. As we described above, the cone collimator for the detector can reduce the scattered photons entering into the detector and, as a result, makes the gold peaks more prominent compared to the background. The same effects of the cone collimator have been shown in the spectra obtained from the simulations with either unfiltered source or filtered source. The scattered photons in the background were reduced with the increase in the size of the collimator opening, while the intensity of the gold fluorescence peaks was unaltered. Besides, the filtered source always produced much more prominent gold peaks because scattered photons due to low energy photons in the beam were significantly suppressed by the filter.
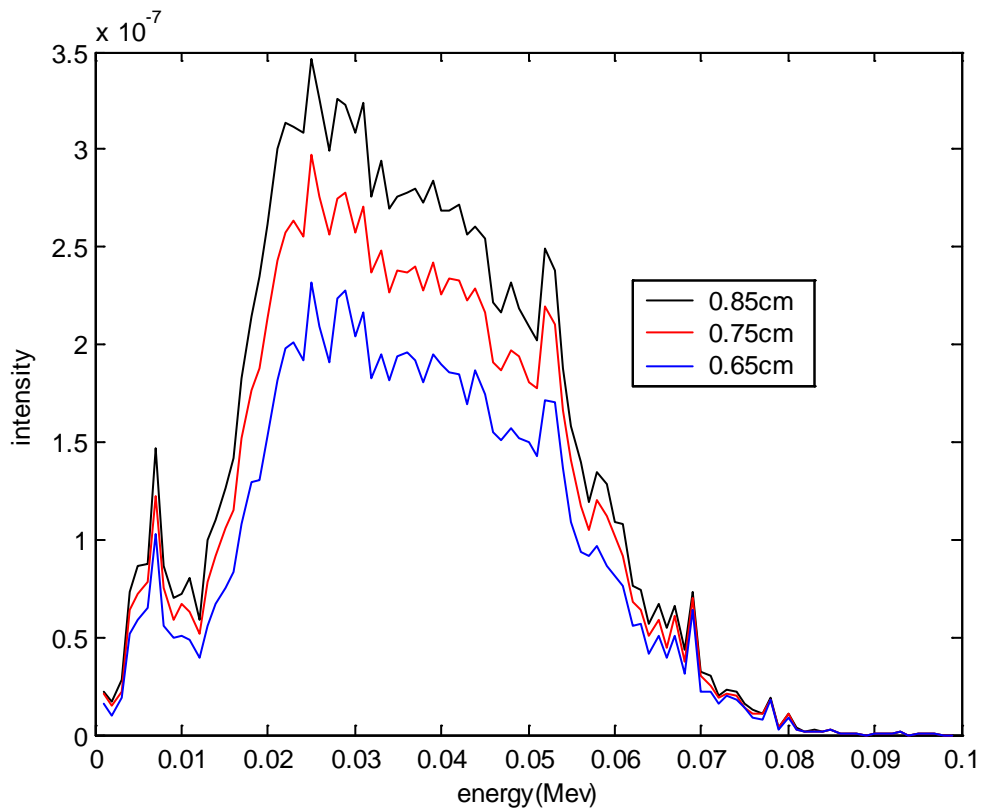
Figure 3.7: Spectra detected from the simulation using three different sizes of the collimator opening for the detector (unfiltered disk source)
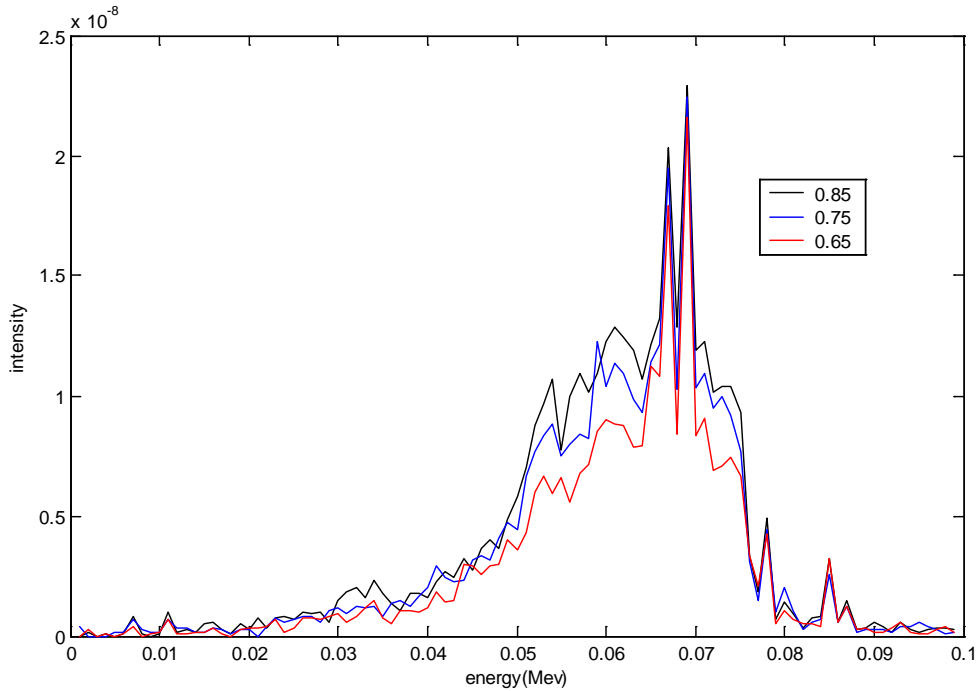
Figure 3.8: Spectra detected from the simulation using three different sizes of the

collimator opening for the detector (filtered disk source)

3.2.2 The Phantom to Detector Distance

We moved our detector towards and away from the phantom to investigate the dependence on the phantom-to-detector distance. Also, both the MCNP simulation and experiment results were acquired and shown in the figures below. As we can see, both the scattered photons and gold fluorescence photons were reduced to the same extent as the phantom to detector distance increased. A comparison shown in Figure 3.13 was made by adjusting the results from the simulation and experiment to the same scale. We can see that our simulation results presented the same curve shape and gold peak localization as those from experiments. Besides, our simulation produced the low-intensity gold peaks which could not be seen in experimental results due to a more complex scattering environment involved with experiments than our MCNP model.
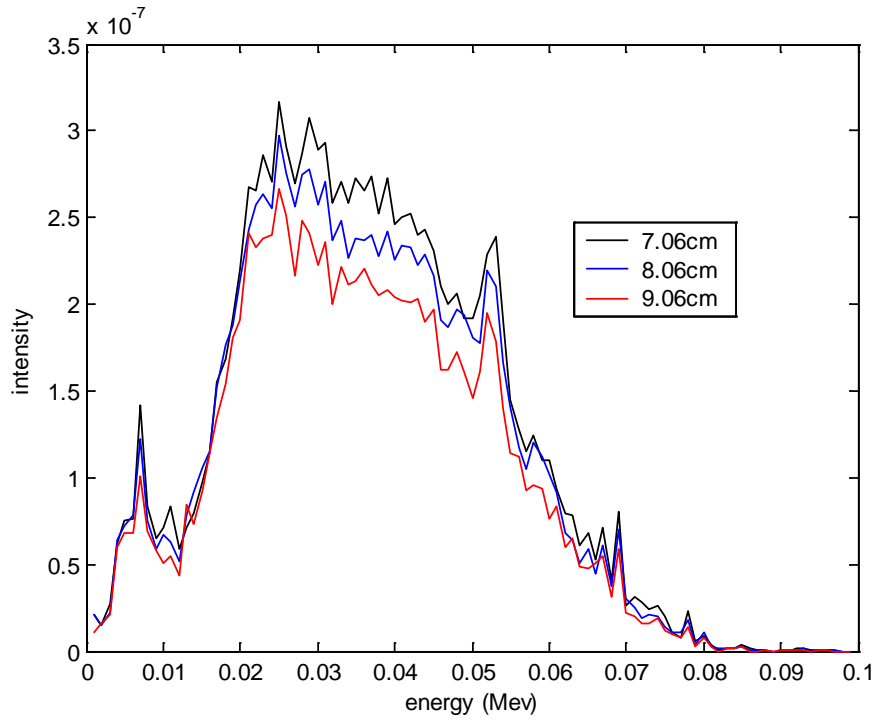
Figure 3.9: Spectra detected from the simulation at three different phantom-to-detector

distances (unfiltered disk source)
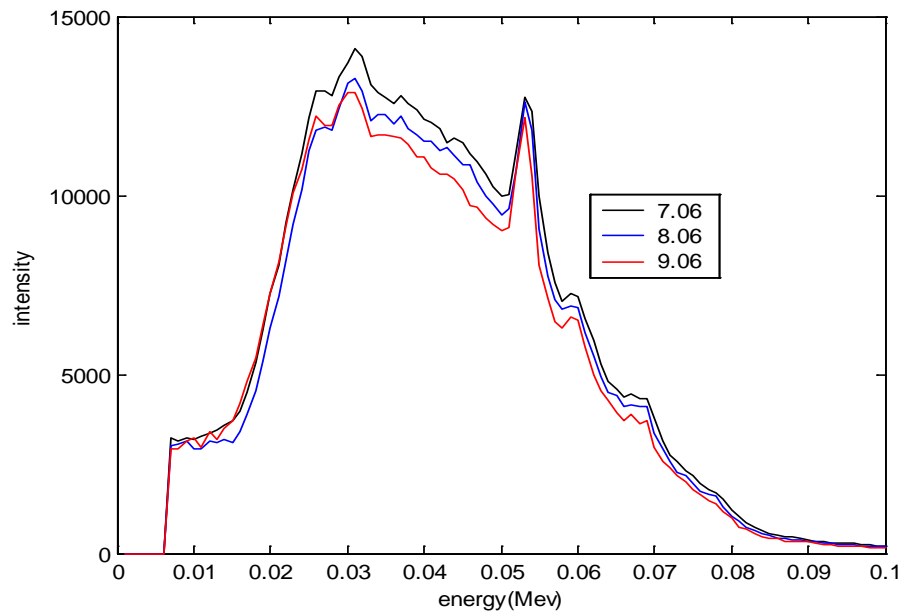
Figure 3.10: Spectra detected from the experiments at three different phantom-to-detector

distances (unfiltered source)
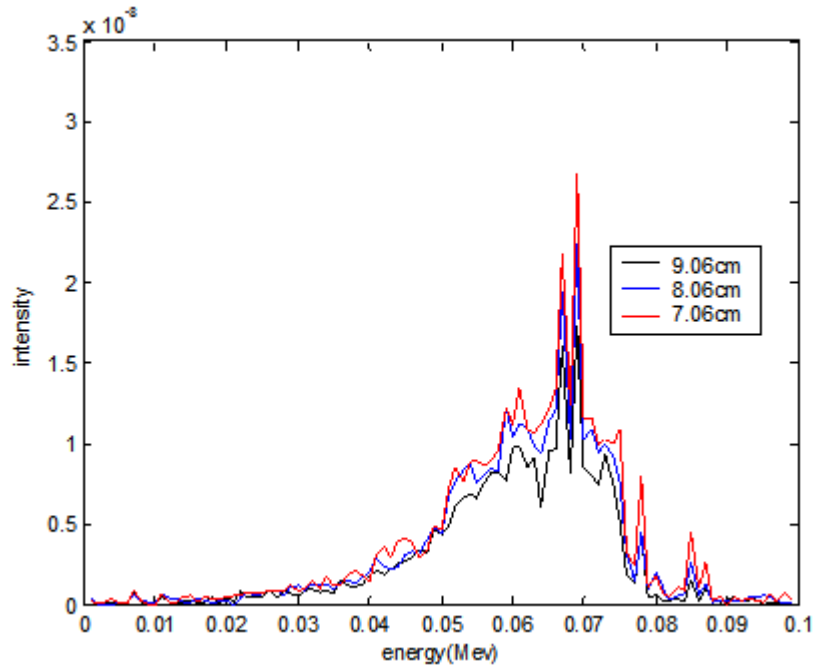
Figure 3.11: Spectra detected from the simulation at three different phantom-to-detector

distances (filtered disk source)
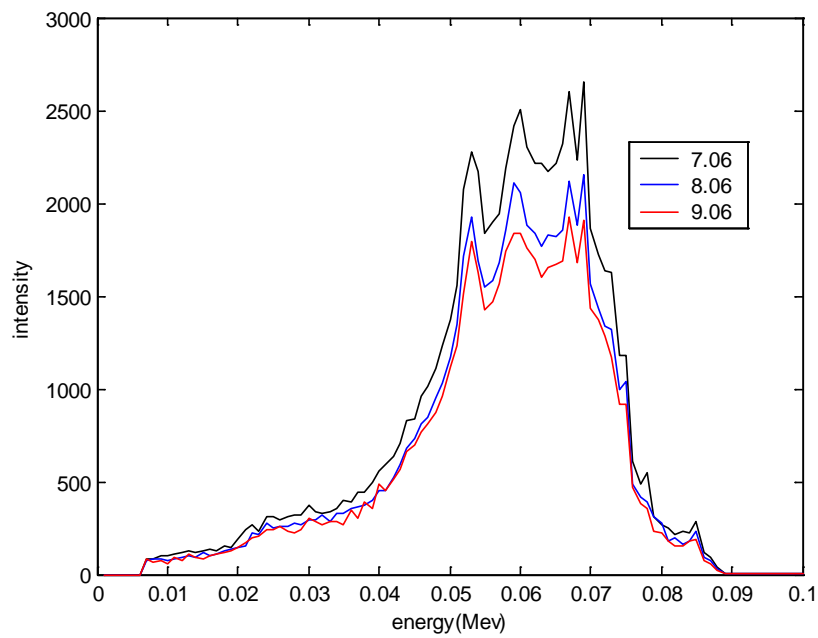
Figure 3.12: Spectra detected from the experiments at three different phantom-to-detector

distances (filtered source)

24
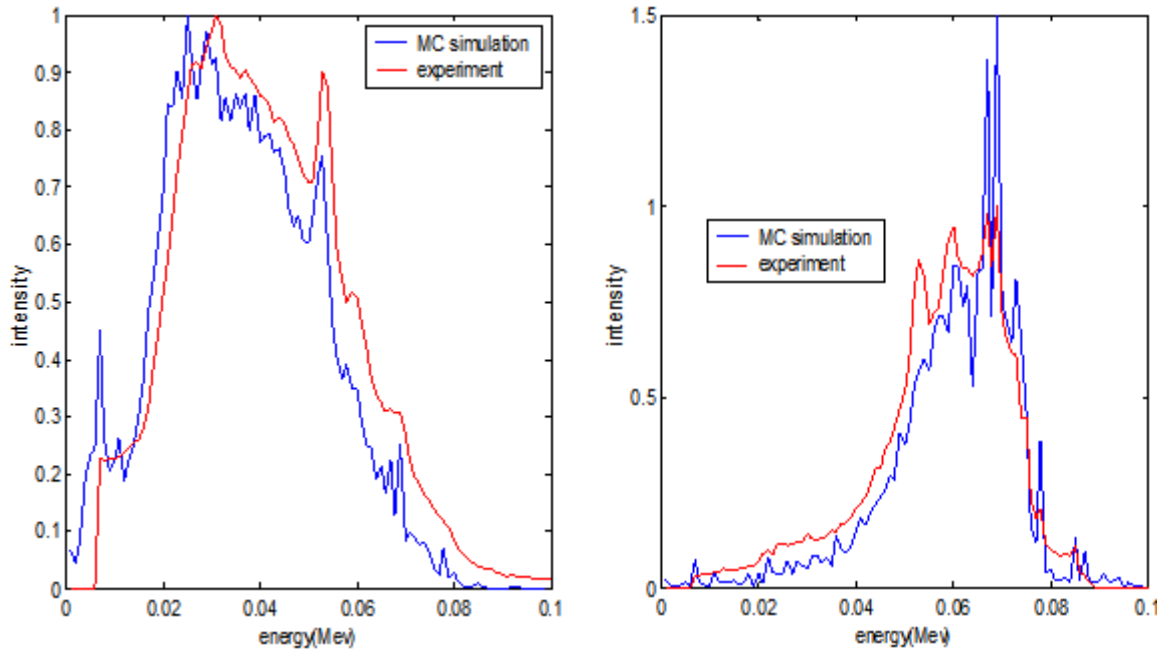
Figure 3.13: Comparison of the spectra detected from Monte Carlo simulations and experiments (the left-side for unfiltered source and the right-side for filtered source)

3.2.3 The Fluorescence Detection Angle

We located the detector at three different fluorescence detection angles (60°, 90° and 120°; see Figure 3.14) to investigate the dependence on the detection angle. The results from the MCNP simulations and the experiments have been acquired under the same condition and shown in the figures below. As we can see from the results, the spectra acquired by the detector located at the forward direction of 60° shows much more scattered photons than those detected at the side direction of 90° and the backward direction of 120°. Besides, the intensity of the gold peaks recorded at the larger off-axis angles was not attenuated much compared to the reduction of the scattered photons. So the detector at larger off-axis angles appears to produce the spectrum with much more prominent gold peaks. Also, the comparison of the simulation and the experimental

results in Figure 3.19 below shows that our simulation can produce the results comparable to experimental results.
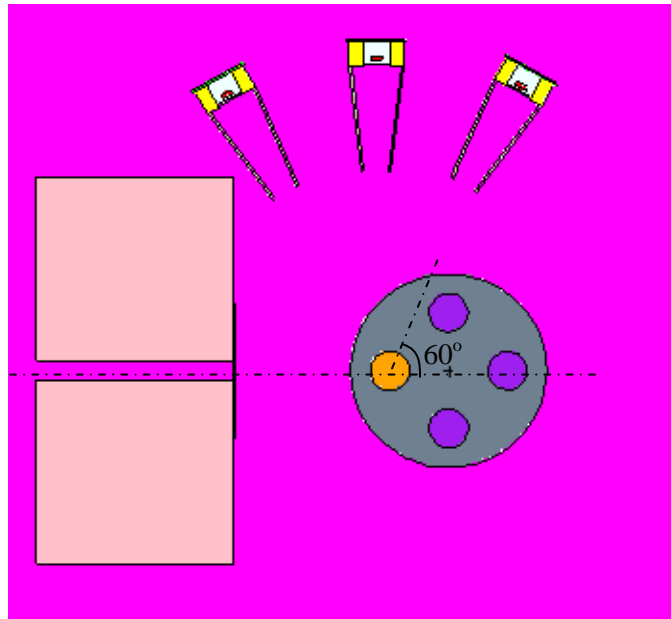
Figure 3.14: The geometry for locating the detector at different fluorescence detection

angles (60°, 90° and 120°)
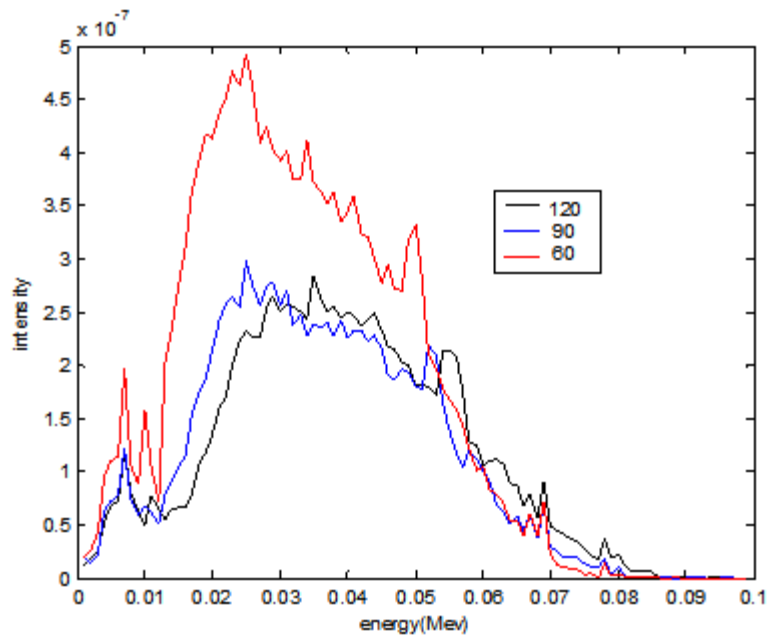
Figure 3.15: Spectra detected from the simulation at three different off-axis detection

angles (unfiltered disk source)
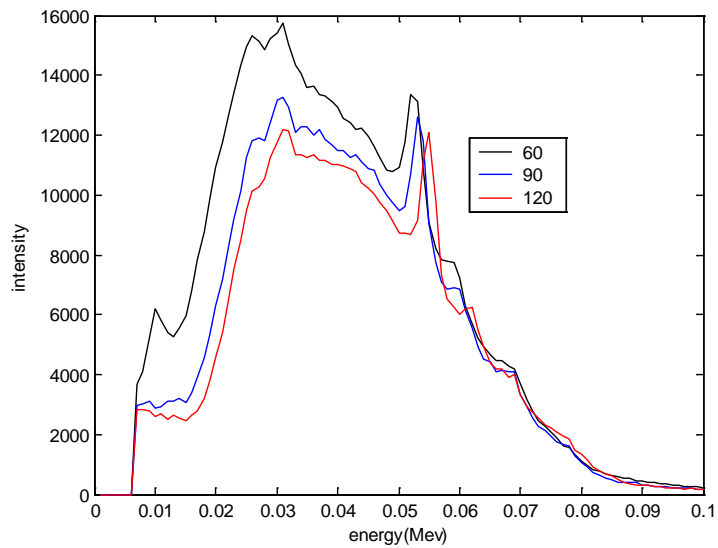
Figure 3.16: Spectra detected from the experiments at three different off-axis detection

angles (unfiltered disk source)
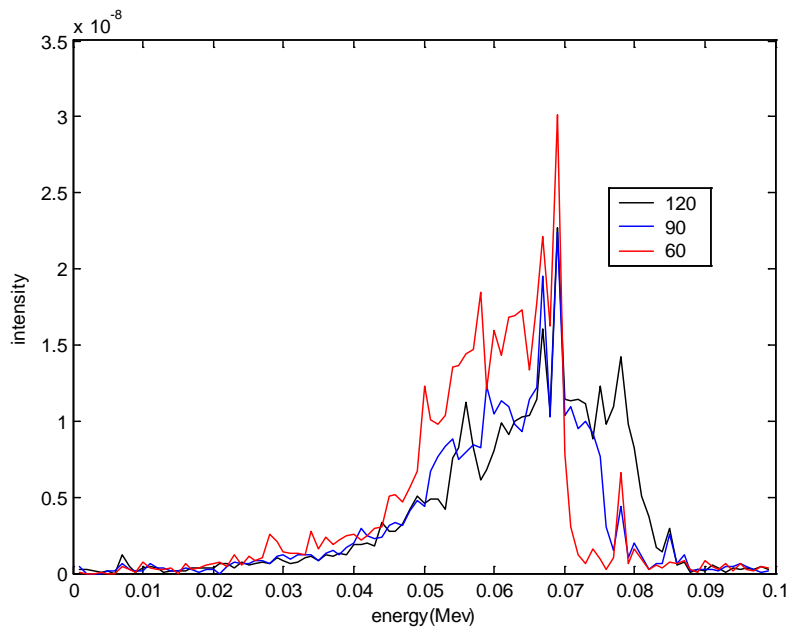
Figure 3.17: Spectra detected from the simulation at three different off-axis detection

angles (filtered disk source)
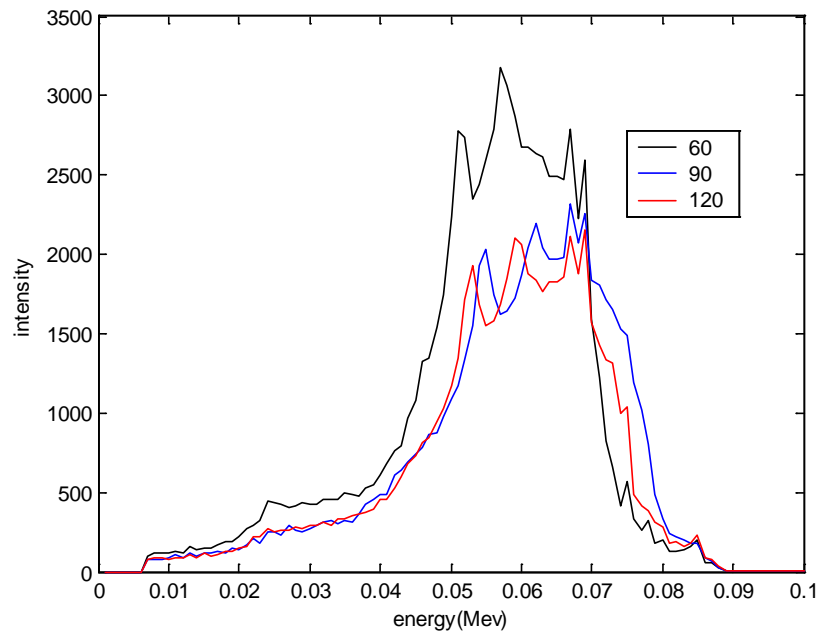
Figure 3.18: Spectra detected from the experiments at three different off-axis detection

angles (filtered disk source)
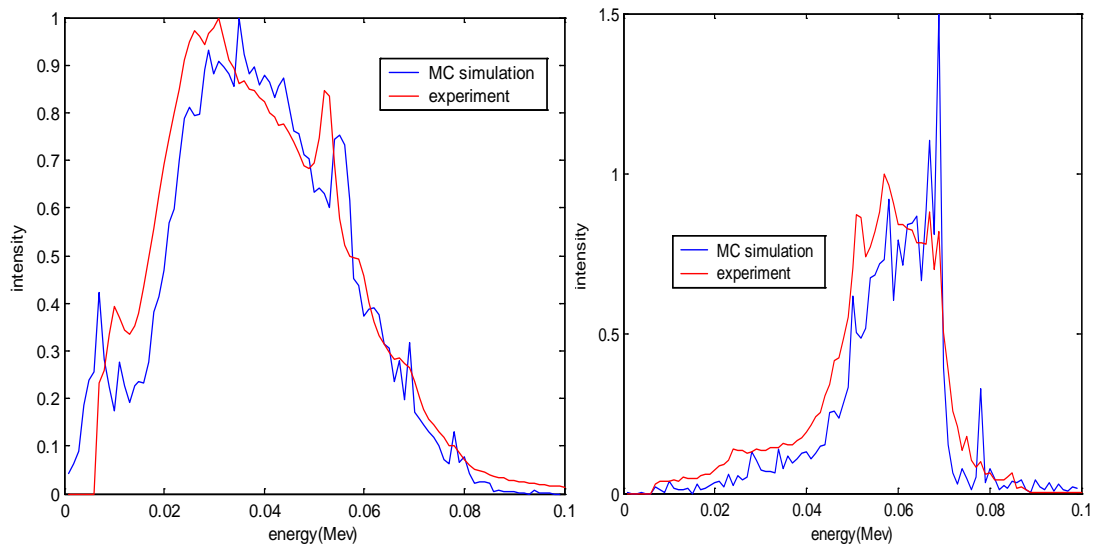
Figure 3.19: Comparison of the spectra obtained from Monte Carlo simulation and

experiments (the left-side for unfiltered source and the right-side for filtered source)

CHAPTER 4

DISCUSSION AND FUTURE WORK

4.1 Discussion

In this work, we divided the simulation task into two steps. The first step was to validate our MCNP model including the source, detector, and the phantom. The second step was to investigate the effect of various model parameters in our MCNP model on the fluorescence detection efficiency, in order to provide some recommendations for further optimization of our future experimental setup.

Every component of the X-ray fluorescence system appears to be properly modeled in our MCNP model according to the simulation results. For example, the cone beam source has been replaced by the disk source right after the source collimator to avoid poor statistics in Monte Carlo results. In addition, a Pb filter has been applied to absorb most of the unnecessary low-energy photons for gold fluorescence X-ray generation. All of these modifications have contributed to the smoothness in the calculated spectra and the distinction of the gold peaks in the spectra as shown in the current results. The detector we modeled was able to detect the gold fluorescence peaks and the height of the peaks was proportional to the concentration of the gold nanoparticles as expected. Besides, a cone collimator for the detector has enabled to obtain more prominent gold fluorescence peaks, because more scattered X-rays from the original X-ray beam and the phantom were discriminated against gold fluorescence X-rays by the collimator. From the testing of the MCNP phantom model, we can see the PMMA material is reasonably tissue-equivalent around the energy range of concern for this work.

Various model parameters have been tested in order to optimize the MCNP model we constructed. The results from MCNP simulations and experiments have been compared and agreed reasonably well. Since the use of the cone collimator for the detector can help reduce the scattered photons, which otherwise would contribute to the spectrum as the scatter noise and bury the gold fluorescence peaks, the size of the opening (i.e., solid angle) is an important design parameter for the detector. As seen from the simulation results, more scattered primary photons can be discriminated against gold fluorescence X-rays by reducing the size of the collimator opening, while a more prominent gold fluorescence peak can be produced. So, in future experiments, we may make the opening of the collimator as narrow as possibly achievable.

Little difference was shown from the testing of the effect of the phantom-to-detector distance on the fluorescence detection efficiency. As we moved the detector closer to the phantom, both the scattered primary photons and the gold fluorescence photons increased to the same extent. So the change of the phantom-to-detector distance has little effect on intensifying the gold fluorescence peak. Both the simulation and experiment results have confirmed this argument. In our simulation, we always located the detector at off-axis angles so that most of the attenuated primary X-rays and some of the scattered primary X-rays could be discriminated so that only scattered primary X-rays and gold fluorescence X-rays were detected. However, different off-axis detection angles produce different spectra. The detector located at 60º off-axis angle resulted in more prominent gold fluorescence peaks than that located at 90º and 120º off-axis angles. This was because most of the scattered photons are directed in the forward and side directions while the fluorescence photons are isotropically emitted from the site of gold

nanoparticles. Therefore, more gold fluorescence photons can be detected at detection angles close to the source, as long as the detector does not directly see the primary photons from the source. Clearly, the results from both the experiment and simulation have proved the above argument. Besides, the spectra from our simulations matched very well with those from the experiments.

4.2 Future Work

As demonstrated so far, the current MCNP model has successfully simulated the X-ray fluorescence system and can accurately determine the gold fluorescence spectra from the phantom. In our future work, we may use it to optimize the experimental tasks to detect X-ray fluorescence from gold nanoparticles for various applications. Especially, our first possible task with this system is to acquire the X-ray fluorescence image data for the image reconstruction. For that, we need to rotate the detector around the phantom at the same degree interval and make several translations at each detection angle. Since we have made a full investigation of the dependence on the detection angle and phantom-to detector distance, the future experimental setup for the X-ray fluorescence imaging will be optimized using the current results and experience. Although it was not attempted during this work, an experimental measurement of the primary spectrum of the 110 kVp X-ray source would facilitate the further development of the current MCNP model for more accurate imaging work. In addition, in order to obtain more accurate results from the simulation, it may be necessary to model those structures presented within our experimental setup but unaccounted for the current model such as electrical parts of the detector, imaging stages and table, etc., which might act as the sources of photon scatter.

Finally, for more elaborated and clinically meaningful experiments such as animal experiments, we will need to model the detailed anatomy of small animals such as a mouse or to adapt an existing model (e.g., digital mouse) and incorporate into the current MCNP model.

CHAPTER 5

CONCLUSIONS

An X-ray fluorescence detection system has been modeled by using the MCNP5 code. An X-ray source, a Pb collimator, a CdTe detector, and an acrylic plastic phantom with four empty cylindrical columns were included in this model. In the simulation, X-rays from a nominal 110 kVp source emitted into a 60° cone from the focal spot of the X-ray source was collimated to a circular beam with a diameter of 5 mm. The collimated beam was then delivered to the plastic phantom with and without a gold nanoparticle-containing column. The fluence of scattered and gold fluorescence X-rays from the phantom was scored within the detector's sensitive volume resulting in various photon spectra which were compared with the measured spectra acquired under the same geometry. Further simulations were performed to investigate the effect of various parameters in our MCNP model on the fluorescence detection efficiency to provide some recommendations for further optimization of our future experimental setup.

The simulation results agreed reasonably well with experimental results suggesting that every component of the X-ray fluorescence system was properly modeled in our MCNP model. The current investigation also suggests that more scattered primary photons can be discriminated against gold fluorescence X-rays by reducing the size of the collimator opening, while a more prominent gold fluorescence peak can be produced. In addition, little difference was shown from the testing of the effect of the phantom-to-detector distance on the fluorescence detection efficiency. Finally, the current results show that more gold fluorescence photons can be detected at detection angles close to the source, as long as the detector does not directly see the primary photons from the source.

The current MCNP model may serve as a useful simulation tool to optimize and troubleshoot experimental tasks necessary for the development of gold nanoparticle-aided cancer detection and therapy procedures.

REFERENCES

[1]   Alex G. Cuenca, Huabei Jiang, Steven N. Hochwald, Matthew Delano, William G. Cance and Stephen R. Grobmyer. Emerging Implications of Nanotechnology on Cancer Diagnostics and Therapeutics, *CANCER*. Vol. 107(3), pp. 459-466, 2006.

[2]   Cho, S. H. Estimation of tumor dose enhancement due to gold nanoparticles during typical radiation treatments: A preliminary Monte Carlo study. *Physics in Medicine and Biology*, Vol. 50(15): N163-N173, 2005

[3]   L. Zhang, S.J. Wilderman, N.H.Clinthorne, and W.L. Rogers. An Anthropomorphic Phantom Integrated EGS4 Monte Carlo Code and Its Application In Compton Probe. *IEE*, Vol. 20, pp. 119-122, 2001.

[4]   Wikipedia, "X-ray fluorescence Homepage: http://en.wikipedia.org/wiki/X ray_fluorescence". Accessed: 9/29/2008

[5]   J. M. Hammersley and D. C. Handscomb. Monte Carlo Methods. Fletcher & Son Ltd, Norwich. 1964.

[6]   Habib Zaidi. Comparative Evaluation of Photon Cross-Section Libraries for Materials of Interest in PET Monte Carlo Simulations. *IEEE TRANSACTIONS ON NUCLEAR SCIENCE*, Vol. 47(6), pp. 2722-2735, 2000.

[7]   J. S. Hendricks and J. F. Briesmeister. Recent MCNP Developments. *IEEE TRANSACTIONS ON NUCLEAR SCIENCE*, Vol. 39(4), pp. 1035-1040, 1992.

[8]   X-5 Monte Carlo Team, "*MCNP-A General Monte Carlo N-Particle Transport Code, Version 5, Volume I: User's Guide*" Los Alamos Controlled Publication, April 24, 2003 (Revised 10/3/05).

[9]   HAMAMATSU company webpage, "Microfocus X-ray Source: http://jp.hamamatsu.com/products/x-ray/pd036/L9631/index_en.html". Accessed: 9/29/2008

[10] Amptek company webpage, "XR-100T-CdTe photon diode detector: http://amptek. com/xr100cdt.html". Accessed: 9/29/2008

[11] H.-E. Nilsson, E. Dubaric, M. Hjelm, K. Bertilsson. Simulation of photon and charge transport in X-ray imaging semiconductor sensors. *Nuclear Instruments and Methods in Physics Research*, Vol. 487,151-162, 2002.

[12] M. Hjelm, B. Norlin, H.-E. Nilsson, C. Fr.ojdh, X. Badel. Monte Carlo simulation of the imaging properties of scintillator-coated X-ray pixel detectors.*Nuclear Instruments and Methods in Physics Research*, Vol. 509, 76-85, 2003.

[13] T. Trojek, T. Cechak. Use of MCNP code in energy dispersive X-ray fluorescence. *Nuclear Instruments and Methods in Physics Research*, Vol. 263, 72-75, 2007.

[14] E. Herrera Peraza, M. Renteria Villalobos, M.E. Montero Cabrera, A. Munoz Romero. X-ray fluorescence analysis in environmental radiological surveillance using HPGe detectors. *Spectrochimica Acta,* Vol. 59 ,1695-1701, 2004.

[15] F.H.H. Al-Ghorabie, S.S.A. Natto, S.H.A. Al-Lyhiani. A comparison between EGS4 and MCNP computer modeling of an in vivo X-ray fluorescence system. *Computers in Biology and Medicine*, Vol. 31, 73-83, 2001.

[16] C. H. Holdsworth, C. S. Levin, M. Janecek, M. Dahlbom, and E. J. Hoffman. Performance Analysis of an Improved 3-D PET Monte Carlo Simulation and Scatter Correction. *IEEE TRANSACTIONS ON NUCLEAR SCIENCE*, Vol. 49(1), 83-89, 2002.

[17] Stephen T. Flock, Brian C. Wilson, and Michael S. Patterson. Monte Carlo Modeling of Light Propagation in Highly Scattering Tissues-11: Comparison with Measurements in Phantoms. *IEEE TRANSACTIONS ON BIOMEDICAL ENGINEERING*, Vol. 36(12). 1169-1173, 1989.

[18] A. Bevilacqua, D. Bollinil, A. Del Guerra, G. Di Domenico, M. Galli, M. Scandola, G.Zavattini. A 3-D Monte Carlo simulation of a small animal Positron Emission tomography with millimeter spatial resolution. *IEEE TRANSACTIONS ON NUCLEAR SCIENCE,* Vol. 46(3), 697-701, 1999.

[19] Florian E. W. Schmidt, Jeremy C. Hebden, Elizabeth M. C. Hillman, Martin E. Fry, Martin Schweiger, Hamid Dehghani, David T. Delpy, and Simon R. Arridge. Multiple-slice imaging of a tissue-equivalent phantom by use of time-resolved optical tomography. *APPLIED OPTICS*, Vol. 39(19), 3380-3387, 2000.